10.2478/msr-2013-0028

Decoupling Analysis of a Sliding Structure Six-axis Force/Torque Sensor

Bo Wu, Ping Cai

Department of Instrument Science and Engineering, Shanghai Jiao Tong University, 200240, Shanghai, China, wb_9941@163.com

This paper analyzes the decoupling of a sliding structure six-axis force/torque sensor, which is used to measure the interactive force between surgical tools and soft tissue for the establishment of soft-tissue force model. Because this decoupling structure requires accurate sliding clearance and symmetric grooves, the influence of contact force between the elastic body and the groove sidewall on decoupling is analyzed. The analysis results indicate that the contact force will produce additional coupling error. The robust design method of elastic body size optimization is used to eliminate the influence of contact force. In the calibration test, the expanded uncertainty of the calibration device is evaluated and the calibration results validate the good decoupling.

Keywords: Tool-tissue interactive force, force/torque sensor, sliding structure, decoupling, robust design, uncertainty.

1. INTRODUCTION

TO IMPROVE the operators' immersion sense in virtual surgery, the haptic information acquisition is carried out to measure the tool-tissue interactive force for the establishment of the soft tissue force model. Many acquisition approaches are based on tensile or compressive test of non-destruction tissue samples [1] [2], which cannot reveal the variation of tool-tissue interactive force for tissue fracture comprehensively [3]-[6]. Many kinds of sensors can be used to measure the force or torque [7]-[10]. Typical surgical operations such as clamping, cutting, puncture and suture feature motion and application of force in a multi-degree of freedom, so multi-axis force/torque sensors are used.

Dimensional coupling elimination is a key issue for multi-axis force/torque sensors. A. Gaillet [11] developed a multi-axis force/torque sensor based on the Stewart parallel structure. But owing to the coupling signal output of the sensor, the calculation of decoupling is complex. For a more direct acquisition of the force signal, the design of some sensors is based on mechanical structure decoupling of the elastic body. Float beam structure and sliding structure are typical mechanical decoupling approaches. A. G. Song [15] developed a kind of float beam structure based multidimensional force sensor. When force is applied, the non-sensing beams of the sensor become floating because of the compliance of non-sensing beams. The dimensional coupling is therefore eliminated. Due to the contradiction between compliance of non-sensing beams and sensor overall stiffness, the decoupling is limited. In the sliding structure based multidimensional force sensor, the non-sensing beams become floating via sliding along the guiding groove, then the decoupling can be more effective. However, this decoupling structure requires accurate sliding clearance and symmetric grooves, especially for the sensor with small measurement range. Otherwise, contact force between the elastic body and the groove sidewall will influence the decoupling.

This research analyzed the mechanical decoupling mechanism of a designed sliding structure six-axis force/torque sensor and the influence of contact force between elastic body and groove on decoupling. The contact force determined by structure size, machining error and assembly error will produce additional coupling error. Owing to the fact that the relationship between contact force and structure size and machining error is non-linear, higher machining and assembly accuracy may not be able to achieve the desired target. Thus, a robust design method [17] of sliding structure for structure size optimization is adopted to eliminate the influence of contact force on decoupling.

2. DECOUPLING ANALYSIS OF THE SLIDING STRUCTURE SIX-AXIS FORCE/TORQUE SENSOR

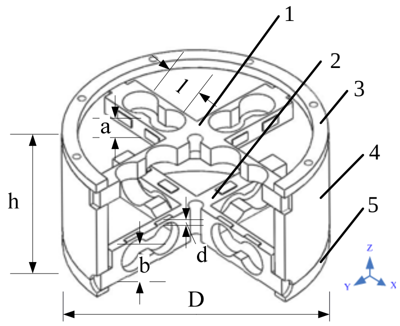

Fig.1. Structure components. (1) elastic body 1, (2) elastic body 2, (3) top cover, (4) outer shell, (5) bottom cover.

The structure components of the six-axis force/torque sensor are shown in Fig.1. Two elastic bodies are composed of four identical parallel beams with double holes, respectively. Elastic body 1 is designed to measure force $\boldsymbol{F}_x$, $\boldsymbol{F}_y$ and torque $\boldsymbol{M}_z$, and elastic body 2 is designed to measure force $\boldsymbol{F}_z$, torque $\boldsymbol{M}_x$ and $\boldsymbol{M}_y$. The clearance fit between the elastic body and the groove of the outer shell makes the elastic body slide when the force is applied. The measurement range of the sensor for force is 0~20 N and for torque is 0~800 Nmm. The resolution of the sensor is 20 mN. The dimension parameters of the sensor are shown in Table 1.

Table 1. Dimension parameters of the sensor

height of the sensor	***h*** = 28 mm
diameter of the sensor	***D*** = 52 mm
height of elastic body 1	***a*** = 4 mm
height of elastic body 2	***b*** = 8 mm
thickness of the thin wall	***d*** = 0.5 mm
distance between the two holes	***l*** = 8 mm

Four strain gauges bonded to the thin wall of each parallel beam of the elastic body compose a full Wheatstone bridge, thus 32 strain gauges and eight full Wheatstone bridges are needed in total. Each parallel beam can measure a single dimensional force, so two or four beams can be combined to measure the same force/torque for increased sensor sensitivity.

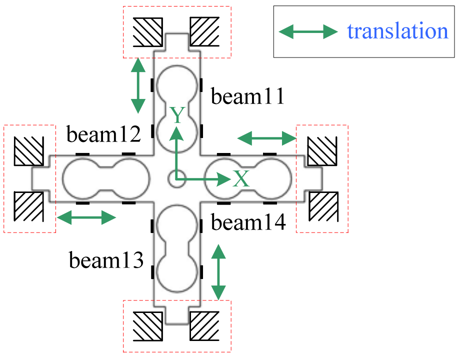

(a) Sliding mechanism of elastic body 1

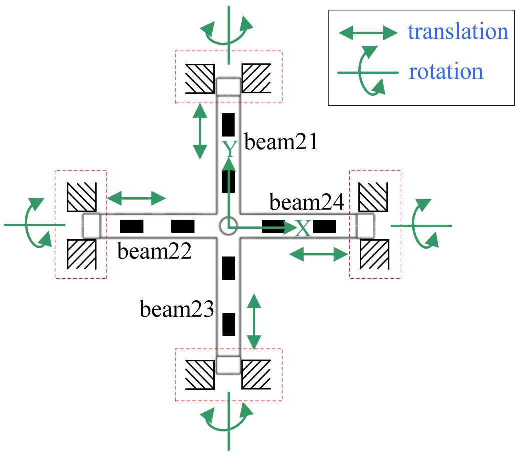

(b) Sliding mechanism of elastic body 2

Fig.2. Sliding structure of the six-axis force/torque sensor

The sliding structure of elastic body 1 and elastic body 2 is shown in Fig.2.(a) and Fig.2.(b), respectively. When a single dimensional force or torque is applied, sensing beams produce bending deformation and non-sensing beams are floating owing to sliding, or produce lateral bending deformation, or torsional deformation.

When bending deformation occurs on beams, there are symmetrical tensile strain and compressive strain on two thin walls on both sides of the beam, respectively. The sensitivity of output voltage can be increased 4 times with the Wheatstone bridge.

When lateral bending deformation occurs on beams, the overall strain of the strain gauge is zero due to the equal tension and compression on both sides of the strain gauge neutral layer, so beams will not sense lateral bending deformation.

When torsion deformation occurs on beams, both normal stress and shear stress are produced in the cross section simultaneously. Because of the great torsional stiffness of beams, the normal strain is very small and can be neglected. The strain gauges do not sense shear deformation, thus beams will not sense torsional deformation.

Thus, beams of the elastic body can sense bending deformation but are insensitive to lateral bending deformation and torsional deformation. The deformation of each beam under a single dimensional force or torque is listed in Table 2.

Table 2. shows that beam 11 and beam 13 sense the deformation under the force $\boldsymbol{F_x}$; beam 12 and beam 14 sense the deformation under the force $\boldsymbol{F_y}$; beam 11, beam 12, beam 13 and beam 14 sense the deformation under the torque $\boldsymbol{M_z}$; beam 21 and beam 23 sense the deformation under the torque $\boldsymbol{M_x}$; beam 22 and beam 24 sense the deformation under the torque $\boldsymbol{M_y}$; beam 21, beam 22, beam 23 and beam 24 sense the deformation under the force $\boldsymbol{F_z}$.

The output can be calculated by

$$\frac{\vec{U}_o}{U_i} = \frac{K}{4}\vec{\varepsilon} \tag{1}$$

where $\vec{\varepsilon} = (\varepsilon_1, \varepsilon_2, \varepsilon_3, \varepsilon_4, \varepsilon_5, \varepsilon_6, \varepsilon_7, \varepsilon_8)$ and $\vec{U}_o = (U_{o1}, U_{o2}, U_{o3}, U_{o4}, U_{o5}, U_{o6}, U_{o7}, U_{o8})$ are the strain and the bridge output voltage of beam 11, beam 12, beam 13, beam 14, beam 21, beam 22, beam 23 and beam 24, respectively, $\boldsymbol{K}$ is the gauge factor, and $\boldsymbol{U_i}$ is the input voltage of the Wheatstone bridge.

Considering the equal deformation of some beams under a single dimensional force or torque, $\vec{U}_F = (U_{Fx}, U_{Fy}, U_{Fz}, U_{Mx}, U_{My}, U_{Mz})$ can be obtained as

$$\vec{U}_F = \begin{bmatrix} 1 & 0 & 1 & 0 & 0 & 0 & 0 & 0 \\ 0 & 1 & 0 & 1 & 0 & 0 & 0 & 0 \\ 0 & 0 & 0 & 0 & 1 & 1 & 1 & 1 \\ 0 & 0 & 0 & 0 & 1 & 0 & -1 & 0 \\ 0 & 0 & 0 & 0 & 0 & 1 & 0 & -1 \\ 1 & 1 & -1 & -1 & 0 & 0 & 0 & 0 \end{bmatrix} \vec{U}_O \tag{2}$$

(2) indicates that the sensor is structure decoupling and the sensor sensitivity is doubled or quadrupled.

Table 2. Deformation under a single dimensional force or torque

	Deformation mode ("B", "-B", "LB", "T" denote tensile bending deformation, compressive bending deformation, lateral bending deformation and torsional deformation and "0" means no deformation)							
	beam 11	beam 12	beam 13	beam 14	beam 21	beam 22	beam 23	beam 24
F_x	B	0	B	0	LB	0	LB	0
F_y	0	B	0	B	0	LB	0	LB
F_z	LB	LB	LB	LB	B	B	B	B
M_x	LB	T	LB	T	B	0	-B	0
M_y	T	LB	T	LB	0	B	0	-B
M_z	B	B	-B	-B	LB	LB	LB	LB

3. INFLUENCE OF CONTACT FORCE ON DECOUPLING

Contact force between the elastic body and the groove sidewall will emerge as a coupling force during the operation. Considering the small measurement range (0~20 N and 0~800 Nmm) of the sensor, it is necessary to analyze the influence of the clearance and the asymmetric groove.

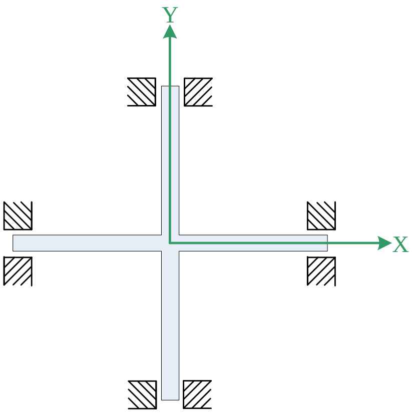

(a) Ideal contact

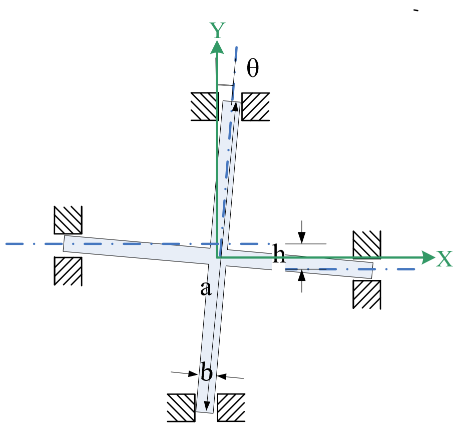

(b) Contact with an angle

Fig.3. Typical contact modes between the elastic body and the groove.

Fig.3.(a) shows the ideal contact mode between the elastic body and the groove. Fig.3.(b) shows the contact mode with angle $\boldsymbol{\theta}$ and deviation distance $\boldsymbol{h}$ of groove, where the deviation distance of the groove is $h = a\sin\theta$. In Fig.3.(b), the branch force might deform the non-sensing beam to bring additional coupling.

The structure of Fig.3.(b) can be equivalent to a first-order hyperstatic structure of sliding structure in order to calculate the bending moment distribution of each beam, which can produce the bending deformation, as depicted in Fig.4.

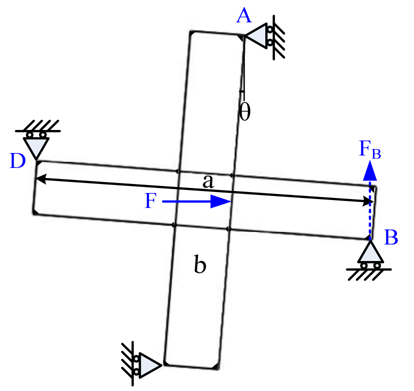

(a) Mechanical model of elastic body 1

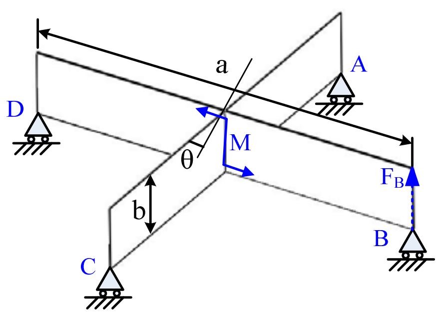

(b) Mechanical model of elastic body 2

Fig.4. First-order hyperstatic structure of the elastic body in the sliding structure.

As shown in Fig.4.(a), four unknown restraint reaction forces and a horizontal force $\boldsymbol{F}$ are applied on the elastic body 1. A redundant vertical reaction force $\boldsymbol{F_B}$ emerges after removing the restraint at endpoint B. The force deformation compatibility condition can be given as

$$\delta_{11}F_B + \delta_{1F} = 0 \tag{3}$$

where δ_{11} and δ_{1F} denote the deformation value of the endpoint B in $\boldsymbol{F_B}$ direction when force $\boldsymbol{F_B}$ and $\boldsymbol{F}$ are applied to the statically determinate base, respectively. δ_{11} and δ_{1F} can be obtained according to Mohr' s theorem, and the vertical reaction force $\boldsymbol{F_B}$ is derived from (3)

$$F_B = K_1 F = \frac{M\sin 2\theta}{N\sin(2\theta+\alpha) + 2(a^3+b^3)/3 + a^2b + ab^2/2}F \tag{4}$$

where

$$M = \sqrt{((a^3-b^3)/6 + a^2b + ab^2)^2 + b^6/4}\,,$$

$$\tan\alpha = ((a^2b - ab^2)/2 - b^3/12)/(a^2b + ab^2/2)\,,$$

$$N = \sqrt{(a^2b + ab^2/2)^2 + ((a^2b - ab^2)/2 - b^3/12)^2}\,.$$

For $\boldsymbol{M} > \boldsymbol{N}$, it is clear that $\boldsymbol{K_1}$ and $\boldsymbol{F_B}$ increase with the increase of θ. The bending moment of all beams, which is produced by the horizontal force $\boldsymbol{F}$ and the vertical reaction force $\boldsymbol{F_B}$, can be obtained based on the superposition principle. The strain of elastic body 1 is given as

$$\varepsilon_5 = \varepsilon_7 = \frac{FL}{2EW}(\cos\theta + K_1\sin\theta) \tag{5a}$$

$$\varepsilon_6 = \varepsilon_8 = \frac{FL}{2EW}(\sin\theta + K_1\cos\theta) \tag{5b}$$

$$\varepsilon_1 = \varepsilon_2 = \varepsilon_3 = \varepsilon_4 = 0 \tag{5c}$$

Assuming $\boldsymbol{F}$ is applied in $\boldsymbol{x}$ direction, $\vec{U}_F$ can be calculated in accordance with (1) and (2)

$$\vec{U}_F = \frac{FLKU_i}{4EW}\begin{bmatrix}(\cos\theta + K_1\sin\theta)\\(\sin\theta + K_1\cos\theta)\\0\\0\\0\\0\end{bmatrix} \tag{6}$$

It follows that force $\boldsymbol{F_x}$ and $\boldsymbol{F_y}$ emerge when force $\boldsymbol{F}$ is applied in $\boldsymbol{x}$ direction, and force $\boldsymbol{F_y}$ is considered as a coupling force. The coupling error $\boldsymbol{E_r(F_x)}$ can be given as

$$E_r(F_x) = \frac{(\sin\theta + K_1\cos\theta)}{(\cos\theta + K_1\sin\theta)} \tag{7}$$

From (4) $0 \le K_1 < 1$ is obtained, then $\Delta\sin(\theta) > K_1\Delta\sin(\theta)$ and $\Delta\cos(\theta) > K_1\Delta\cos(\theta)$ is derived. (6) and (7) indicate that the contact angle produces additional coupling. The coupling error $\boldsymbol{E_r(F_x)}$ increases with the increase of θ.

When moment $\boldsymbol{M}$ is applied on elastic body 2, the mechanical model is shown in Fig.4.(b). Similar method to that of elastic body 1 can be used to obtain the bending moment distribution. Assuming $\boldsymbol{M}$ is applied in $\boldsymbol{x}$ direction, $\vec{U}_F$ can be obtained as

$$\vec{U}_F = \frac{FLKU_i}{4EW}\begin{bmatrix}0\\0\\0\\(\sin\theta + K_2\sin\theta)\\(\sin\theta + K_2\cos\theta)\\0\end{bmatrix} \tag{8}$$

where $K_2 = \dfrac{27ab\sin\theta}{21ab + 10a^2}$.

The coupling error $\boldsymbol{E_r(M_x)}$ produced by ε_{My} can be given as

$$E_r(M_x) = \frac{(\sin\theta + K_2\sin\theta)}{(\cos\theta + K_2\sin\theta)} \tag{9}$$

(9) shows that the coupling error $\boldsymbol{E_r(M_x)}$ increases with the increase of θ.

4. Robust optimization design of sensor sliding structure

Robust optimization design approach is used to ensure good quality performance when controllable factors and uncontrollable factors deviate from the design value. This approach aims to minimize the performance sensitivity to noise by selecting the appropriate design parameters instead of eliminating the noise factor.

If the coupling error change caused by controllable factors and uncontrollable factors is allowed, the decoupling of sliding structure is robust. For sliding structure of the sensor, the size of the elastic body $\boldsymbol{a}$, $\boldsymbol{b}$ and the groove width $\boldsymbol{r}$ are given as undetermined random variables and feature Gaussian distribution. The design variables (controllable factors) are shown as

$$\mathbf{x} = (a,b,r)^T = (x_1, x_2, x_3)^T .$$

Δa, Δb and Δr are machining errors, and noise factors (uncontrollable factors) are shown as

$$\mathbf{z} = (\Delta a, \Delta b, \Delta r)^T = (z_1, z_2, z_3)^T .$$

$\mathbf{x} \sim (\boldsymbol{\mu}_{\mathbf{x}}, (\Delta\mathbf{x}/3)^2)$ can be obtained, where $\boldsymbol{\mu}_{\mathbf{x}}$ is expectation of $\boldsymbol{x}$.

The coupling error $\boldsymbol{y}$ is determined by both controllable factors and uncontrollable factors and can be obtained as

$$y = E_r(F_x) = y(\mathbf{x}, \mathbf{z}) \tag{10}$$

$\boldsymbol{y}$ is design target function and the ideal value is 0. The statistical mean $\bar{y}$ can approach the target value via expectation $\mu_y \to \min$ and Δy can be minimized via variance $\sigma_y \to \min$. The target function with smaller-the-better can be established as

$$\min F(\mathbf{x}, \mathbf{z}) = \mu_y + \beta\sigma_y \tag{11}$$

where β is weighted coefficient for coordination of expectation and variance. Adding constraint function $g(\mathbf{x})$, the robust optimization model can be given as

$$\begin{cases} \mathbf{x} = (x_1, x_2, x_3)^T \\ \min F(\mathbf{x}, \mathbf{z}) = \mu_y + \beta\sigma_y \\ s.t. g(\mathbf{x}) = x_1^2 + x_2^2 - x_3^2 \geq 0 \\ x_1 \in (45, 55), x_2, x_3 \in (3, 5) \end{cases} \tag{12}$$

The initial value, discrete increments and upper and lower bounds of design variables are listed in Table 3. $\beta = 0.97$ and $(\Delta x_1, \Delta x_2, \Delta x_3) = (0.046, 0.022, 0.022)$ (GB/T 1800.3-1998 IT8) are given. μ_y and σ_y can be calculated based on best square approximation method after sampling. When $y = E_r(M_x) = y(\mathbf{x}, \mathbf{z})$, the same method can be used.

The robust optimization design solution can be obtained by using one-dimensional traversal optimization. The optimized sizes of elastic body are shown in Table 4., and the corresponding mean and variance of random function $\boldsymbol{E_r(F_x)}$ and $\boldsymbol{E_r(M_x)}$ is 0.34 % and 0.48 % for elastic body 1, and 0.65 % and 0.72 % for elastic body 2, respectively.

Table 3. The initial value, discrete increments, upper and lower bounds of design variables

Variables (mm)	Discrete increments	Upper bound	Lower bound
$x_1(a)$	0.010	55	45
$x_2(b)$	0.001	5	3
$x_3(r)$	0.001	5	3

Table 4. Robust result of optimized design variables

	a	b	r	Δa	Δb	Δr
elastic body 1 (mm)	52.041	4.732	4.758	0.046	0.022	0.022
elastic body 2 (mm)	51.386	4.260	4.309	0.046	0.022	0.022

5. CALIBRATION TEST

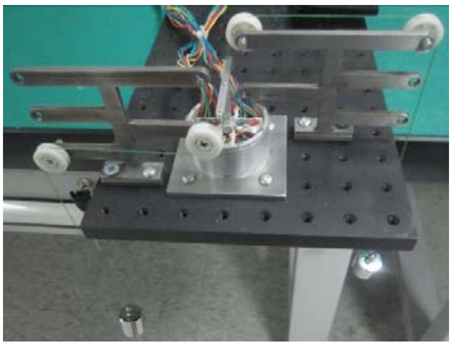

Fig.5. Calibration device of sensor (torque $\boldsymbol{M_x}$ calibration)

The uncertainty is a parameter that reasonably shows the dissolution characteristic of a measurement value [23]. Fig.5. shows the calibration test of the fabricated six-axis force/torque sensor. In the calibration of the six-axis force/torque sensor, the combined standard uncertainty is obtained by combining the A type standard uncertainty due to lack of reproducibility, the B type standard uncertainty from the calibration device. The B type standard uncertainty due to the resolution of the data acquisition card.

In order to calculate the uncertainty due to lack of reproducibility, the force $\boldsymbol{F_x}$, $\boldsymbol{F_y}$ and $\boldsymbol{F_z}$ from 1 N to 20 N at 1 N steps, and torque $\boldsymbol{M_x}$, $\boldsymbol{M_y}$ and $\boldsymbol{M_z}$ from 40 Nmm to 800 Nmm at 40 Nmm steps is measured, respectively, five times. The full-scale output voltage is 10 V. The average measured values at each step are obtained and the standard deviation $\boldsymbol{S}$ of the force $\boldsymbol{F_x}$, $\boldsymbol{F_y}$ and $\boldsymbol{F_z}$, and torque $\boldsymbol{M_x}$, $\boldsymbol{M_y}$ and $\boldsymbol{M_z}$ can be calculated with the maximum average measured value from Bessel formula. The uncertainty $\boldsymbol{u_r}$ can be expressed as

$$u_r = \frac{S}{\sqrt{5}} \tag{13}$$

The calculated uncertainty $\boldsymbol{u_r}$ of the force $\boldsymbol{F_x}$, $\boldsymbol{F_y}$ and $\boldsymbol{F_z}$, and torque $\boldsymbol{M_x}$, $\boldsymbol{M_y}$ and $\boldsymbol{M_z}$ is 0.0037 V, 0.0035 V, 0.0029 V, 0.0046 V, 0.0047 V and 0.0052 V, respectively. The freedom $\boldsymbol{v_r}$ = 5-1 = 4.

The uncertainty from the calibration device means the uncertainty due to the transmission of force and torque. The maximum force direction deviation angle α during the calibration can be measured. Multiplying the coverage factor $\boldsymbol{k} = \sqrt{3}$, the uncertainty $\boldsymbol{u_f}$ from the calibration device can be expressed as

$$u_f = \frac{U_o(1-\cos\alpha)}{\sqrt{3}} \tag{14}$$

Where $\boldsymbol{U_o}$ is the measured output voltage of $\boldsymbol{F_x}$, $\boldsymbol{F_y}$, $\boldsymbol{F_z}$, $\boldsymbol{M_x}$, $\boldsymbol{M_y}$ or $\boldsymbol{M_z}$.

The calculated uncertainty $\boldsymbol{u_f}$ of the force $\boldsymbol{F_x}$, $\boldsymbol{F_y}$ and $\boldsymbol{F_z}$, and torque $\boldsymbol{M_x}$, $\boldsymbol{M_y}$ and $\boldsymbol{M_z}$ is 0.0013 V, 0.0012 V, 0.0009 V, 0.0013 V, 0.0015 V and 0.0018 V. The freedom $\boldsymbol{v_f} = \infty$.

The revolution of the data acquisition card is 0.0003 V. Multiplying the coverage factor $\boldsymbol{k} = \sqrt{3}$, the uncertainty $\boldsymbol{u_d}$ due to the resolution of data acquisition card can be calculated as 0.0003 V/$\sqrt{3}$=0.00018 V. The freedom $\boldsymbol{v_d} = \infty$.

The combined standard uncertainty $\boldsymbol{u_c}$ can be written as

$$u_c = \sqrt{u_r^2 + u_f^2 + u_d^2} \tag{15}$$

The calculated uncertainty $\boldsymbol{u_c}$ of the force $\boldsymbol{F_x}$, $\boldsymbol{F_y}$ and $\boldsymbol{F_z}$, and torque $\boldsymbol{M_x}$, $\boldsymbol{M_y}$ and $\boldsymbol{M_z}$ is 0.0039 V, 0.0037 V, 0.0030 V, 0.0048 V, 0.0049 V and 0.0055 V. The freedoms of $\boldsymbol{F_x}$, $\boldsymbol{F_y}$, $\boldsymbol{F_z}$, $\boldsymbol{M_x}$, $\boldsymbol{M_y}$ and $\boldsymbol{M_z}$ are 4.

The expanded uncertainty $\boldsymbol{U}$ is calculated by multiplying the combined uncertainty $\boldsymbol{u_c}$ by the coverage factor $\boldsymbol{k}$ = 1.9 (confidence level 95%, $\boldsymbol{t_{0.95}}$ (4) = 1.9). The equation for it can be written as

$$U = ku_c \tag{16}$$

The calculated expanded uncertainty $\boldsymbol{U}$ of $\boldsymbol{F_x}$, $\boldsymbol{F_y}$, $\boldsymbol{F_z}$, $\boldsymbol{M_x}$, $\boldsymbol{M_y}$ and $\boldsymbol{M_z}$ is 0.0074 V, 0.0070 V, 0.0057 V, 0.0091 V, 0.0093 V and 0.01 V, respectively.

The following relationship between force and output voltage can be given

$$\vec{F} = [D]\vec{U}_F \tag{17}$$

where $\vec{F} = (F_x, F_y, F_z, M_x, F_y, F_z)$, **[*D*]** is the static calibration matrix.

During the calibration procedure of the force/torque sensor, the force $\boldsymbol{F_x}$, $\boldsymbol{F_y}$ and $\boldsymbol{F_z}$ are applied to the sensor from 1 N to 20 N at 1 N steps, respectively, and the torque $\boldsymbol{M_x}$, $\boldsymbol{M_y}$ and $\boldsymbol{M_z}$ are applied to the sensor from 40 Nmm to 800 Nmm at 40 Nmm steps, respectively. In the meantime, the voltage output values of the bridge from eight beams are recorded and 480 calibration data are obtained in total. $\vec{U}_F$ can be calculated from (2) and the static calibration matrix **[*D*]** can be calculated from (17) with least squares fitting as

$$[D] = \begin{bmatrix} 370.15 & -0.01 & -1.99 & -1.88 & 1.71 & -1.79 \\ 0.92 & 409.28 & -2.39 & -3.54 & -1.52 & -3.17 \\ -0.14 & -0.57 & 86.44 & -0.35 & -0.65 & -0.32 \\ -7.98 & -5.67 & -4.82 & 1082.8 & -2.98 & -4.78 \\ -8.91 & -9.34 & -5.42 & -2.62 & 1051.3 & -7.57 \\ -6.38 & -9.33 & 7.99 & -6.84 & -4.79 & 2708.2 \end{bmatrix} \tag{18}$$

The static calibration matrix indicates that the coupling errors of $\boldsymbol{F_x}$ are between 0.01 % and 0.54 %; the coupling errors of $\boldsymbol{F_y}$ are between 0.22 % and 0.86 %; the coupling errors of $\boldsymbol{F_z}$ are between 0.16 % and 0.75 %; the coupling errors of $\boldsymbol{M_x}$ are between 0.28 % and 0.74 %; the coupling errors of $\boldsymbol{M_y}$ are between 0.25 % and 0.89 %; the coupling errors of $\boldsymbol{M_z}$ are between 0.18 % and 0.34 %. The maximum coupling error of the developed six-axis force/torque sensor is 0.89 % and the minimum coupling error is 0.01 %. It can be said that the measurement sensitivity is 5.4 mV/N for $\boldsymbol{F_x}$ and $\boldsymbol{F_y}$, 4.2 mV/N for $\boldsymbol{M_x}$ and $\boldsymbol{M_y}$, 4.8 mV/Nmm for $\boldsymbol{F_z}$ and 5.3 mV/Nmm for $\boldsymbol{M_z}$.

6. CONCLUSIONS

In this paper, the decoupling mechanism of a designed sliding structure six-axis force/torque sensor is analyzed. This sensor can decouple more thoroughly, for each beam of elastic body can only sense a single dimensional force/toque independently. Because of sliding clearance and asymmetric groove, elastic body will come into contact with the groove at a certain angle. Thus, contact force will be applied to the non-sensing beams of elastic body and produce additional coupling error. The contact angle is related to structure size of the sensor, machining error and assembly error. Robust optimization method was employed by optimizing the elastic body size a, b, and the groove width r to eliminate the coupling error but not decrease the machining error. The calculated values a, b and r are 52.041 mm, 4.732 mm and 4.785 mm for elastic body 1, and 51.386 mm, 4.260 mm and 4.309 mm for elastic body 2, respectively. For calibration device, the calculated expanded uncertainty of $\boldsymbol{F_x}$, $\boldsymbol{F_y}$, $\boldsymbol{F_z}$, $\boldsymbol{M_x}$, $\boldsymbol{M_y}$ and $\boldsymbol{M_z}$ is 0.0074 V, 0.0070 V, 0.0057 V, 0.0091 V, 0.0093 V and 0.01 V, respectively, with 10 V full-scale output voltage. The corresponding mean and variance of coupling error is 0.34 % and 0.65 % for elastic body 1, and 0.48 % and 0.72 % for elastic body 2, respectively. The calibration test was carried out and the results show that the coupling errors are between 0.01 % and 0.89 %.

7. ACKNOWLEDGEMENT

This work was supported by grant no. 2009AAZ313 from National High-tech R&D Program of China (863 Program) and by the project of the Basic theory and key technology research of surgical virtual simulation and surgical evaluation from the National Natural Science Foundation, project number: 61190124.

REFERENCES

[1] Fung, Y.C. (1993). *Biomechanics: Mechanical Properties of Living Tissues* (2nd ed.). New York: Springer.

[2] Bummo Ahn, Jung Kim. (2007). An efficient soft tissue characterization method for haptic rendering of soft tissue deformation in medical simulation. In *Frontiers in the Convergence of Bioscience and Information Technologies (FBIT 2007),* 11-13 October 2007. IEEE, 549-553.

[3] Greenish, S., Hayward, V., Steffen, T., Chial, V., Okamura, A.M. (2002). Measurement, analysis and display of haptic signals during surgical cutting. *Presence*, 11 (6), 626-651.

[4] Chanthasopeephan, T., Desai, J.P., Lau, A.C.W. (2003). Measuring forces in liver cutting for reality-based haptic display. In *IEEE/RSJ International Conference on Intelligent Robots and Systems,* 27-31 October 2003. IEEE, 3083-3088.

[5] Frick, T.B., Marucci, D.D., Cartmill, J.A., Martin, C.J., Walsh, W.R. (2001). Resistance forces acting on suture needles. *Journal of Biomechanics*, 34 (10), 1335-1340.

[6] Hu, T., Tholey, G., Desai, J.P., Castellanos, A.E. (2004). Evaluation of a laparoscopic grasper with force feedback. *Surgical Endoscopy*, 18 (5), 863-867.

[7] Kumar, A., Kumar, H. (2011). Stability studies of torque transducers. *Measurement Science Review,* 11 (2), 41-44.

[8] Liu, X.h, Jin, L. (2011). Effect of the volume of magneto-rheological fluid on shear performance. *Measurement Science Review,* 11 (2), 53-56.

[9] Sadana, S., Yadav, S., Jha, N., Gupta, V.K., Agarwal, R., Bandyopadhyay, A.K., Saxena, T.K. (2011). A computer controlled precision high pressure measuring system. *Measurement Science Review,* 11 (6), 198-202.

[10] Abu_Al_Aish, A., Rehman, M., Abdullah, M.Z., Abu Hassan, A.H. (2010). Microcontroller based capacitive mass measuring system. *Measurement Science Review,* 10 (1), 15-18.

[11] Gaillet, A., Reboulet, C. (1983). An isostatic six components force and moment sensor. In *Proceedings of the 13th International Symposium on Industrial Robotics*.

[12] Ke-Jun Xu, Cheng Li. (2000). Dynamic decoupling and compensating methods of multi-axis force sensors. *IEEE Transactions on Instrumentation and Measurement*, 49 (5), 935–941.

[13] Sheng A. Liu, Hung L. Tzo. (2002). A novel six-component force sensor of good measurement isotropy and sensitivities. *Sensors and Actuators A: Physical*, 100 (2-3), 223–230.

[14] Huang Weiyi, Jiang Hongming, Zhou, Hanqing. (1993). Mechanical analysis of a novel six-degree-of-freedom wrist force sensor. *Sensor and Actuators A: Physical*, 35 (3), 203-208.

[15] Aiguo Song, Juan Wu, Gang Qin, Weiyi Huang. (2007). A novel self-decoupled four degree-of-freedom wrist force/torque sensor. *Measurement*, 40 (9-10), 883-891.

[16] Pham Huy Hoang, Vo Doan Tat Thang. (2010). Design and simulation of flexure-based planar force/torque sensor. In *IEEE Conference on Robotics Automation and Mechatronics (RAM),* 28-30 June 2010. IEEE, 194-198.

[17] Mauro Da Lio. (2010). Robust design of linkages - synthesis by solving non-linear optimization problems. *Mechanism and Machine Theory*, 32 (8), 921-932.

[18] Gab-Soon Kim, Hi-Jun Shin, Jungwon Yoon. (2008). Development of 6-axis force/moment sensor for robot's intelligent foot. *Sensors and Actuators A: Physical*, 141 (2), 276–281.

[19] Kim, H.-M., Yoon, J., Kim, G.-S. (2012). Development of a six-axis force/moment sensor for a spherical-type finger force measuring system. *IET Science, Measurement & Technology,* 6 (2), 96-104.

[20] Weichao Yang, Bo Song, Yong Yu, Yunjian Ge. (2008). Design of a micro six-axis force sensor based on double layer E-type membrane. In *International Conference on Information and Automation (ICIA 2008)*, 20-23 June 2008. IEEE, 1632–1636.

[21] Gab-Soon Kim. (2007). Design of a six-axis wrist force/moment sensor using FEM and its fabrication for an intelligent robot. *Sensors and Actuators A: Physical*, 133 (1), 27–34.

[22] International Organisation for Standardisation. (1995). *Guide to the Expression of Uncertainty in Measurement (GUM)*

Received December 6, 2012.
Accepted July 25, 2013.